Mapping the Electromagnetic Near Field of Gold Nanoparticles in Poly(methyl) Methacrylate

By

Kristin Jean Engerer

Thesis

Submitted to the Faculty of the

Graduate School of Vanderbilt University

in partial fulfillment of the requirements

for the degree of

MASTER OF SCIENCE

in

Interdisciplinary Materials Science

December, 2016

Nashville, Tennessee

Approved:

Richard Haglund. Ph.D.
Jason Valentine, Ph.D.

ACKNOWLEDGEMENTS

TABLE OF CONTENTS

LIST OF FIGURES

CHAPTER 1

Introduction

Motivation

For the past forty years, electronic devices have gotten faster and more complex in design

and function. To support this trend, the components to build such devices have had to become

increasingly smaller and faster themselves, which has prompted a great deal of innovation on the

part of scientists and engineers. However, many people believe that the physical limitations of

the basic materials used to create all of these advances in electronics are being reached.
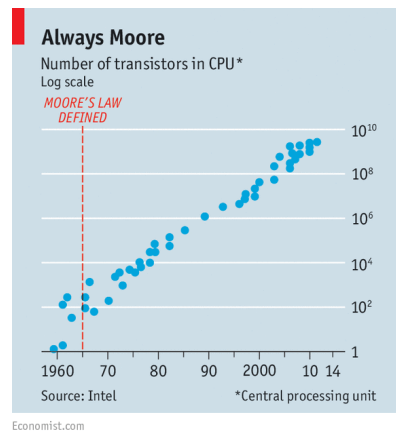
Figure 1: Moore's law- the number of transistors in a device will double every 18-24 months[1]. Used with permission

Scientists have started to look in new directions to continue the miniaturization of

electronic devices. One of the most popular of these new directions is to utilize electromagnetic

(EM) fields instead of electric fields that drive electron currents, with devices transmitting

information using the flow of light instead of the flow of electrons. There are two main branches

within this research. One is to create optical analogs of electronic devices, such as transistors and

inductors. The other is to develop devices that take advantage of the unique properties of electromagnetism and can be used to enhance the functionality of other devices. In this document I will examine in brief the current state of the field of optical analysis tools and provide a deeper analysis of one particular technique: mapping electromagnetic near fields in poly(methyl) methacrylate (PMMA). This analysis will lay the groundwork for developing that technique into a quantitative analytical tool for the design of plasmonic nanoantennas.

Plasmonics and Nanoantennas

A conventional conductor functions because electrons are mobile. In a conductive material, electrons in the conduction band are not bound to specific positive ions as they are in an insulator. Therefore, when voltage is applied to the system, electrons are able to travel through the material away from the applied negative voltage. This current is the basis of electricity and conventional electronic devices.

Since the mobile electrons in the conduction band are free to move, they will fluctuate about their average positions even when no voltage is applied. These oscillatory fluctuations can be described by an average frequency called the the plasma frequency (see Eqn 1 below). Following the derivation outlined in *Optical Properties of Solids*[2]:

$$\omega_p = \left(\frac{Ne^2}{\epsilon_0 m_0} \right)^{1/2} \qquad\qquad \text{Eqn 1}$$

Classical physics can be used to derive the equations of motion for these electrons in the presence of an oscillatory electromagnetic field at frequency ω, which describe the movements of electrons in the presence of these fields in both transverse and longitudinal directions.

$$\frac{\partial^2 \boldsymbol{E}_t}{\partial t^2} + \omega_p^2 \boldsymbol{E}_t - c^2 \nabla^2 \boldsymbol{E}_t = 0 \qquad\qquad \text{Eqn 2}$$

$$\frac{\partial^2 \mathbf{E}_l}{\partial t^2} + \omega_p^2 \mathbf{E}_l = 0 \qquad\qquad \text{Eqn 3}$$

The dispersion relation for a wave-like transverse mode is:

$$c^2 k^2 = \omega^2 - \omega_p^2. \qquad\qquad \text{Eqn 4}$$

These modes will not be able to travel through the material because the waves will be reflected by the surrounding plasma. The solution in the longitudinal direction, on the other hand, is simply:

$$\omega = \omega_p, \qquad\qquad \text{Eqn 5}$$

This shows that longitudinal modes can exist, and in fact correspond to the zeros of the dielectric function. Considering the system in a non-classical manner, we see that the system behaves as a harmonic oscillator, and therefore the energy of the plasma oscillations is quantized in units of $\hbar\omega_p$. The quasi-particles corresponding to the quantized plasma oscillations are known as plasmons (see Fig 2).
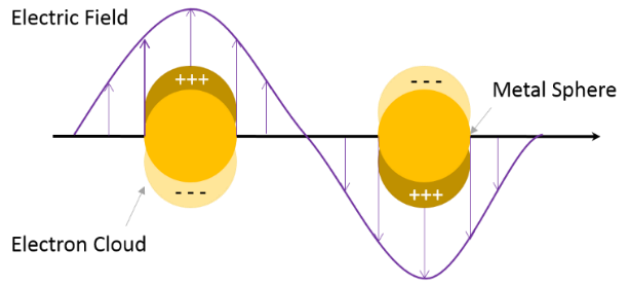
Figure 2: Schematic of a plasmon. Electrons in a metal nanoparticle oscillate in phase with the electric field applied to them

Plasma oscillations are induced by applying an external electromagnetic field. For electrons in a bulk metal, only longitudinal modes can couple to incoming energy This means that light is not an effective means of driving these fields, as light exists as a transverse wave; scattering would be required to excite longitudinal modes from a transverse wave. However, a

second type of plasmon can be seen at the interface between a metal and a dielectric material, known as a surface plasmon. These plasmons have both longitudinal and transverse components (see Fig 3), which means that photon fields can be used to induce plasmonic effects. The system of coupled light and plasma oscillations is quite strong, and is referred to as a surface plasmon polariton (SPP).
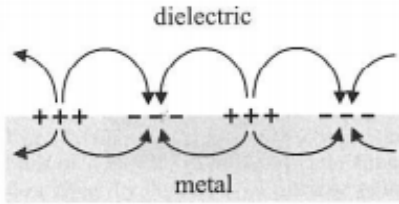
Figure 3: Electric fields associated with electron charge density flucuations[2]

When surface plasmons dominate over bulk plasmons, the effects can be observed, and therefore utilized, more easily. Very small metal particles, called nanoparticles, have a high surface-to-volume ratio, and the effects of surface plasmons will be stronger. Instead of being able to travel along the surface of the metal, as surface plasmon polaritons do, the surface fields are confined to the nanoparticle itself. This is known as a localized surface plasmon (LSP). At particular wavelengths, LSP oscillations can experience resonant enhancement and cause the optical properties of the metal to shift. Examining the polarizability for these plasmons, we can learn why the resonance in optical properties occurs.

$$\alpha = 4\pi a^3 \frac{\epsilon_m - \epsilon_d}{\epsilon_m + 2\epsilon_d}. \hspace{3cm} \text{Eqn 6}$$

In this equation α is the polarizability, a is the size of the nanoparticle, ϵ_m is the dielectric function of the metal, and ϵ_d is the dielectric function of the surrounding dielectric material. The polarizability will be maximized when $Re[\epsilon_m] = -2Re[\epsilon_d]$. This means that as the plasmon is confined to the nanoparticle, a resonance will be established and the system will react more

strongly to applied fields. Therefore, optical absorption will be enhanced and will occur at a different frequency than in the bulk material.

All plasmonic nanoparticles exhibit the resonant enhancement and shifting of the absorbance band from the bulk to the surface resonance mentioned above, but the plasmonic response depends on the material of which they are made, the material in which they are embedded, and the size of the nanoparticle (see Eqn 6). Because of this variability, scientists can obtain vastly different properties and different overall responses simply by changing the design of the nanoparticles used and the material of the surrounding medium.

Two separate nanoparticle systems will be considered in this document: the dipole antenna and the bowtie antenna. Dipole antennas consist of a single rectangular bar or nanorod (See Fig 4, a) while bowtie antennas consist of two triangles pointed towards each other, separated by a narrow gap (Fig 4, b).
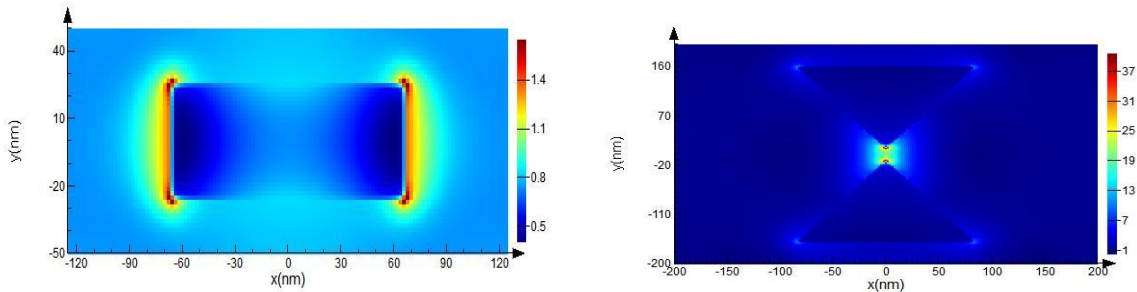
Figure 4: (a) Dipole antenna. (b) Bowtie antenna. In each figure, the scale is normalized to the applied field.

Methods of Characterization

As the previous discussion has shown, optical devices are designed with quite different parameters than conventional electronic devices. Instead of considering the input voltage and the resistance of the device in question, scientists need to consider the frequency of the input light and the refractive index of the material used. Moreover, the size of optical devices must change

depending on what frequency of light is being utilized. For example, in one experiment in which control of radiation in the microwave region (1 mm–1µm) was observed, an array of split-ring resonators of 1.5 mm in radius and standard gauge copper wire was used[3].

Visible light has a much shorter wavelengths (390 nm–750 nm); and as such the structures needed to control those waves need to be nanometer sized. (Fig 5) shows the progression of optical device size over time. Since it is a great deal more challenging to fabricate a nanometer-scale device than a millimeter-scale device, devices designed to guide light in the microwave region were the first ones to be experimentally realized[3]. Current top-down lithographic techniques allow the fabrication of few-nanometer-scale devices, but no smaller. New fabrication techniques will be required to pass the current size limit.
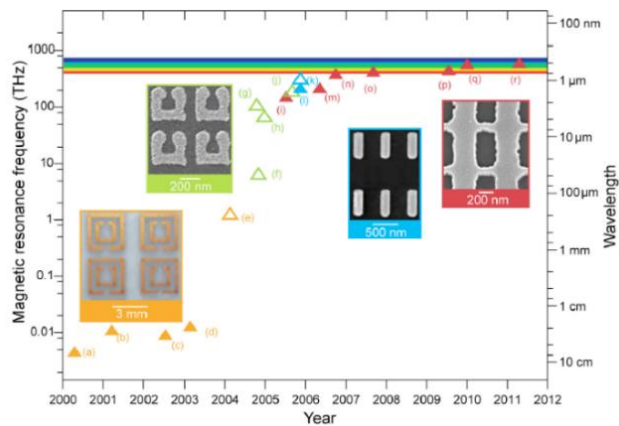
Figure 5: Optical device size reduction over time

Due to the nature of an optical device, most conventional methods for characterizing an electronic device would be either inefficient or would simply not work at all. Therefore, new methods of characterization for these devices have been developed. The first of these characterization techniques, and still one of the most common, is scanning near-field optical microscopy, SNOM. Scientists using conventional, optical microscopes discovered that it was

impossible to distinguish two adjacent features that were closer together than about 200 nm. The

problem occurred due to the diffraction of light rays as they travelled through the microscope.

This became known as the diffraction limit, and in 1873 Ernst Abbé formalized the problem[2].

When imaging two objects in a light microscope, the closest that the two objects can be to each

other and still be resolved is given by:

$$d = \frac{\lambda}{2n \sin \theta}$$
<div align="right">Eqn 7</div>

This means that with 500 nm wavelength light travelling through air at normal incidence, the

smallest resolvable feature is about 250 nm. If two objects smaller than that are close to each

other, they will be indistinguishable from a single larger object. However, by having the light

pass through a subwavelength diameter aperture that is located very close to the imaged features,

this limit can be bypassed.

In the original demonstration, a piece of quartz was fabricated to a sharp tip and coated in

metal[4]. The metal at the very tip was then removed to create the tiny aperture desired. Current

techniques utilize coated optical fiber to transmit the light onto the sample[5]. This fiber can then

be scanned over the surface to collect information about the samples. (See Fig 6 a)
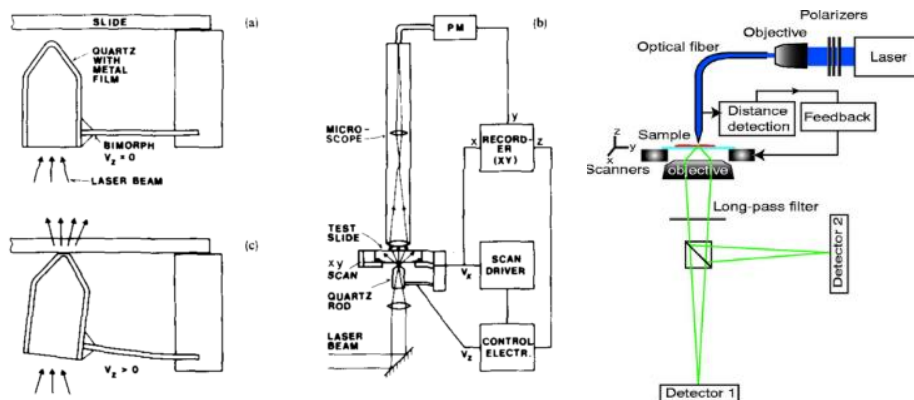
Figure 6: Schematic of SNOM set-ups. (a), (b), and (c) all come from the original demonstration of this technique[4]. (d) is an example of a current SNOM system[5]. Used with permission.

This technique revolutionized the field of microscopy. Countless variations of SNOM were developed to improve the resolution. However, there are still limitations. This technique relies on the excitation and capture of evanescent waves, which contain rich information but only exist very close to the surface of the originating object. Thus the tip must be very close to the object to be imaged, and this can lead to unintended interactions between the object to be imaged and the imaging tip. Scanning near-field optical microscopy has been able to reach a spatial resolution of less than 50 nm, but some applications would still require better resolution than that, including much of the information in the near field of various nanoparticle antennas.

Electron energy-loss spectroscopy (EELS) can improve on the spatial resolution of SNOM by utilizing a beam of electrons rather than a beam of photons and is able to collect maps of plasmons in the near-infrared-visible-ultraviolet domains[6, 7]. Electron beams can also be used to generate cathodoluminescent (CL) radiation, which can be used to determine the dispersion relation of SPPs[8]. All three of these techniques, SNOM, EELS, and CL, are able to provide useful information on different near-field phenomena. However, none of these methods can in fact provide spatial maps of the electromagnetic near field. For that, we must turn to methods that can either image near fields in real time, or techniques that create an image or imprint of the near field that can be observed subsequently in an appropriate microscope.

Prior work in optical near-field mapping

In 2004, Paul Leiderer et al. discussed a method to improve on the current ways to image optical near fields.[9]. He utilized short laser pulses to irradiate different types of nanoparticles, with the intensity of the pulses tailored to cause no damage to the substrate in the far field. If the optical near-field enhancement of the nanoparticles was strong enough, the substrate surface

would be ablated. This damage could then be examined using atomic force microscopy (AFM), capturing a nonlinear "photograph" of the optical near-field intensity distribution.

Leiderer's group examined this effect with both dielectric and metallic nanoparticles. The particles were illuminated with 800 nm light, with pulse duration of 150 fs and energy of ~10 mJ per pulse. The incident light was polarized along the y-axis. A polystyrene sphere was utilized to demonstrate the feasibility for dielectric particles.
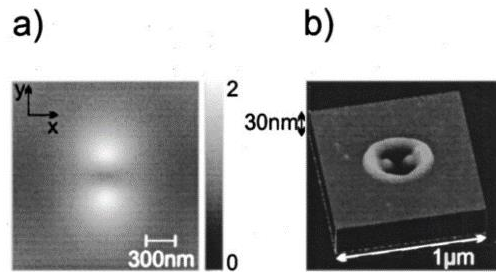
Figure 7: Map of a polystyene nanosphere (a) Calculated near-field intensity profile (b) AFM scan of ablated area[9]. The two areas (light in (a) and dark in (b)) agree well. Used with permission.

Fig 7a shows the calculated optical near-field intensity and Fig 7b shows the AFM scan collected of this system. The ablated area (dark in this image) matches very well with the calculated area expected to be ablated, which shows the quanitative accuracy of this technique.

For metallic particles, Leiderer used an array of gold triangular nanoparticles (Fig 8, a), and once again, the substrate was ablated at points of the highest optical near-field intensities, as shown in Fig 8, c and d.
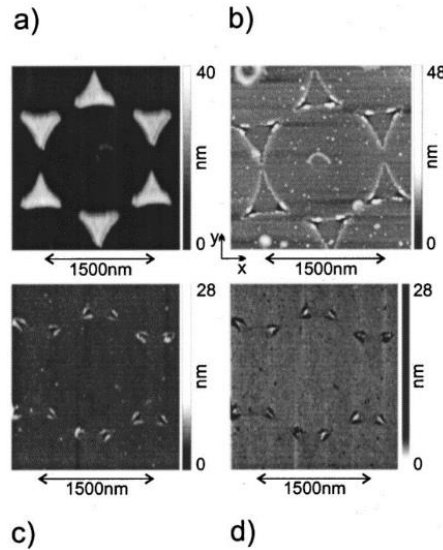
Figure 8: Map of a set of gold nanotriangles. (a) shows the fabricated nanostructures. (b) shows the particles after the laser pulse was applied. (c) shows the mapped field intensity after the remaining gold was removed. (d) is (c) with inverted contrast to make the areas of field intensity appear bright[9]. Used with permission.

This work demonstrated that it was possible to image details of optical near fields with a resolution below the diffraction limit. However, to produce these images, the sample in question has to be destroyed. In the case of the polystyrene sphere, the sphere is etched and worn away when the laser pulse hits it. In the case of the metallic nanoparticles, the metal must be removed to provide clear images of the ablated area. In both cases the substrate itself is the "film" on which the image is captured, making this technique less useful to scientists and engineers wanting to verify the function of their device partway through development.

In 2012, a significant improvement to this technique was made. Rather than inducing ablation in the substrate, Romain Quidant and researchers at the Institute of Photonic Sciences (ICFO) coated metallic nanoantennas in a photosensitive polymer and induced the near-field enhanced damage in that material rather than the material to be imaged.[10]. They used several different near-field antenna geometries and used poly(methyl methacrylate) (PMMA) as the

10

photosensitive polymer. Some of the different near-field resonators were designed to be resonant at wavelengths between 700 nm to 1 μm to determine the most efficient resonant location.
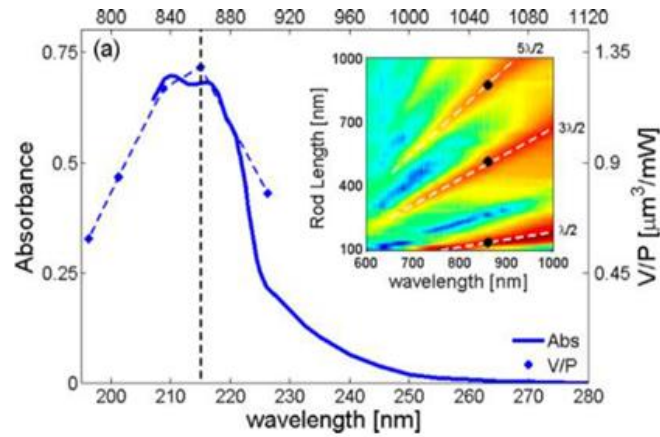
Figure 9: Absorbance spectrum of PMMA and of several gold nanostructures resonant between 700 nm and 1000 nm[10]. Used with permission.

Figure 9 shows the absorbance spectrum for PMMA and an overlay of the absorbance of the different resonant nanoantenna structures. PMMA has an absorbance band centered at 215 nm and the nanoantenna structure with the greatest absorbance is resonant at 860 nm. The fourth harmonic of 860 nm light is 215 nm. This suggests quite strongly that the PMMA is damaged according to a nonlinear process of dielectric breakdown in a highly localized area, which will be discussed in more depth in Chapter 2 of this work. As in Leiderer's work, the laser pulse itself is not able to damage the material. In the previous case the intensity was set to be low enough to avoid ablating the area outside of the near field. In this case the experimenters used a wavelength (860 nm) well outside of PMMA's primary absorbance band, allowing the near-field enhancement to induce the damage in the PMMA but not allowing the PMMA to be damaged elsewhere.
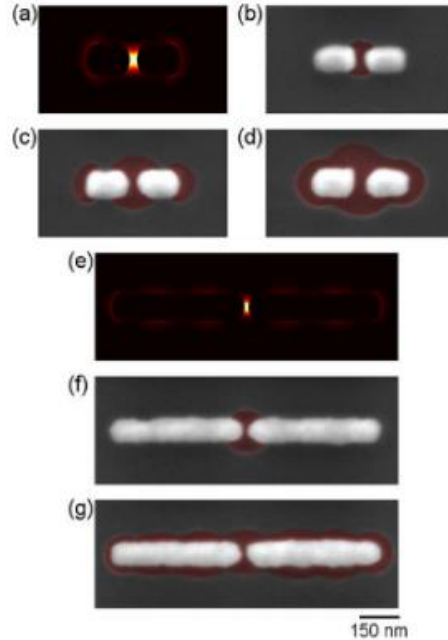
Figure 10: Mapping resonant modes in plasmonic gap antennas. (a) and (e) show simulated electric near-field intensities. (b)–(d) and (f)–(g) show SEM images of exposed PMMA for increasing applied laser intensity. The damaged areas have been highlighted in red[10]. Used with permission.

Once the near fields of the plasmonic nanostructures have damaged the surrounding PMMA, this overlay can be chemically treated to remove the damaged sections and the whole device imaged using an SEM. See Chapter 3 for a description of this preparation. Fig 10 shows these maps, taken at several different input laser intensities. Figures 10a and 10e show the simulated near-field strength for two split-dipole nanorod antennas with different gaps. Figures 10 b–d and f–g show SEM images with added color to enhance the damaged near field region. As the applied intensity increases, the generated field increases in amplitude and the volume of polymer damaged increases. Figure 10c in particular illustrates this well; the region of highest electric field will exist in the gap of the structure, and the largest amount of damaged polymer is observed there. The ends of the dipole will also exhibit field enhancement, so they too register damage, but a lesser amount.
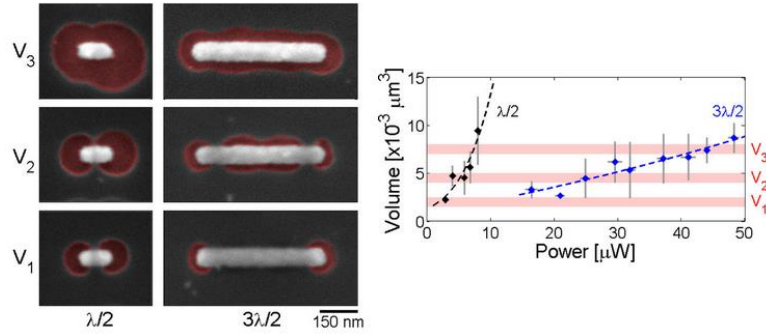
Figure 11: Power dependence of mapped volume. (a) shows three different volumes of polymer, corresponding to the red bands on figure (b). (b) shows a plot of mapped volume to applied power[10]. Used with permission.

Figure 11 shows an examination of power applied *vs* damaged volume measured for two nanorods, one of which is resonant at $\lambda/2$ and the other at $3\lambda/2$, where λl is the wavelength of the laser used to excite the nanorods. The left-hand figure shows maps of two different structures at different applied powers and the right-hand figure shows the plot of the increase in damaged volume as the applied power increases. The volume increases as a high power of the applied field for the $\lambda/2$ nanorod, and in a quasi-linear manner for the $3\lambda/2$ nanorod, which indicates that the technique has the ability to be not only a qualitative technique, used to see where the fields are located, but also a quantitative technique. The technique is currently useful as a way to gauge where the most intense fields will occur; it could be vastly more useful if the damage volume could be calibrated to a specific applied intensity. We will be replicating the results obtained at the ICFO, and using those results as a starting point in the development of the quantitative relationship between the volume of damaged polymer generated when nanointennas are illuminated and the intensity of the light used to illuminate them.

CHAPTER 2

Theory and Simulations

Theory

Quidant showed that PMMA could be used to display the near-field electric-field strength

pattern of a gold antenna[10]. Due to the fact that PMMA has direct absorption at wavelengths of

260 nm and shorter, and Quidant's laser-irradiation experiments were conducted at 860 nm, it is

clear that the photo-induced damage to the nanorod antennas occurred via a nonlinear process.

Hao Jiang and Reuvan Gordon conducted a theoretical study of the six most likely nonlinear

processes that could cause the PMMA to be exposed in the manner observed by Quidant[11]. The

six processes considered are listed below, and can also be seen schematically in Figure 12.
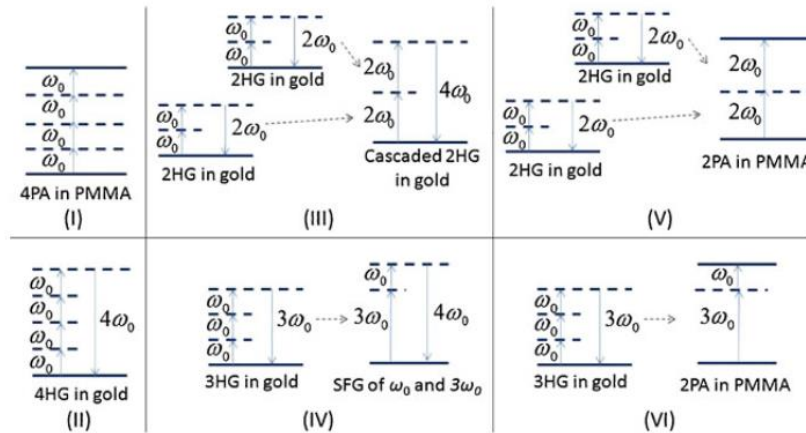
Figure 12: Schematic of primary nonlinear processes that may cause PMMA film to be exposed by 860 nm laser pulses: (I) direct 4PA, (II) direct 4HG, (III) Cascaded 2HG, (IV) SFG of 3HG and FF photons, (V) 2PA of two 2HG photons, and (VI) 2PA of 3HG and FF photons[11]. Used with permission.

I. Direct four-photon absorption (4PA): four 860 nm photons are absorbed directly in

    PMMA

II.   Direct fourth-harmonic generation (4HG): due to the optical nonlinearity at the gold's surface, four 860 nm photons combine in a nonlinear way to produce one 215 nm photon and expose PMMA via linear absorption

III.   Cascaded second-harmonic generation (2HG): two 860 nm photons produce one 430 nm photon through a 2HG process in gold, and subsequently two such 430 nm photons produce one 215 nm photon through another 2HG process in gold. The produced 215 nm photons expose PMMA via linear absorption

IV.   Sum-frequency generation (SFG) of third-harmonic generation (3HG) and the fundamental frequency (FF): three 860 nm photons produce one 287 nm photon via a 3HG process in gold; subsequently through a SFG process, one 287 nm photon and one 860 nm photon produce one 215 nm photon to expose PMMA via linear absorption

V.   Two-photon absorption (2PA) of two second-harmonic generated (2HG) photons: two 860 nm photons produce one photon of 430 nm through a 2HG process in gold; two such 430 nm photons are then absorbed in PMMA via a 2PA process

VI.   Two-photon absorption (2PA) of one third-harmonic generated (3HG) photon and one fundamental frequency (FF) photon: three 860 nm photons produce one 287 nm photon via a 3HG process in gold; one 287 nm photon and one 860 nm photon are then absorbed in PMMA via a 2PA process

Processes I and II are single-step nonlinear processes, while processes III-VI are indirect processes involving two steps. Any processes involving more than two absorption or emission steps will have a much lower probability of occurring. Additionally, the optical absorption of gold is much stronger than that of PMMA, so multiple harmonic generation in PMMA would

logically be weaker than in gold. As such, the strengths of those processes would not be comparable to the above processes.

The probabilities for the processes listed above were studied to determine which one produced an exposure profile that most closely matched those observed by Quidant. A secondary consideration was which process required the lowest laser intensity threshold to produce a given exposure profile. Figure 13 shows the comparison of all six processes based on these two measures. Figure 13a shows a plot of the developed volume vs. time-average laser intensity, which gives the measure of how much or how little light is needed to cause damage to occur. Figure 13b then shows a visual representation of the damage created around an antenna for each process, at two different volumes. From this, it is clear that the exposure profile generated for processes I, II, and VI has the closest match to the experimental data published by Quidant.
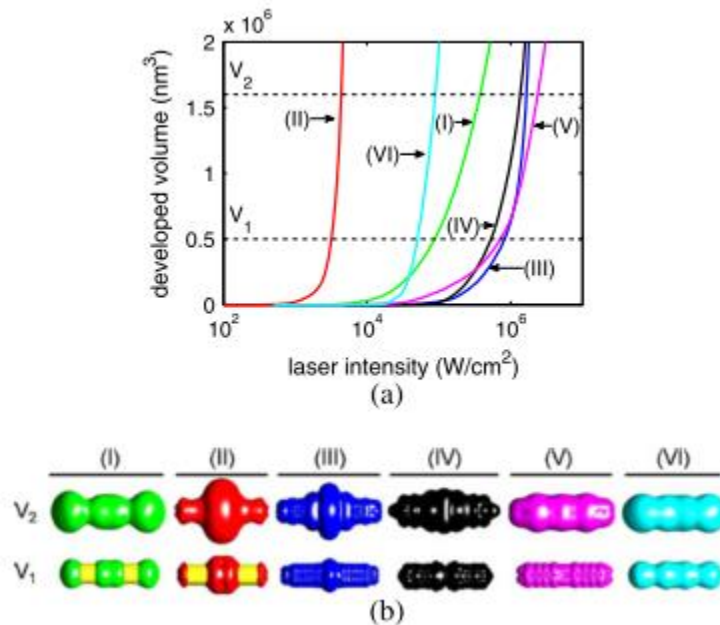
Figure 13: Comparison of the six processes for a gap antenna. (a) shows the developed volume vs. time average laser intensity (b) shows the developed volumes that would be generated for each process at two indicated volumes from (a)[11]. Used with permission.

Process II, which is direct 4HG generation in gold and linear absorption in PMMA, has a threshold laser intensity that is an order of magnitude lower than the other processes. In addition, it has the best agreement with the Quidant experiments as to where the local enhancement would be greatest. Other tests were performed, and it was concluded that direct fourth-harmonic generation at the surface of gold nanoparticles is dominant.

Simulations

Gordon's analysis gave us a greater understanding of how this technique caused the near-field enhancement maps to be generated. With that information, we could move on to replicating the effect. To do so, nanoparticle arrays had to be designed. Our laser has a wavelength centered at 800 nm, so we would be unable to utilize the exact dimensions employed by Romain Quidant. Because of this, several different nanoparticle structures were considered for analysis. The calculations to determine the optimized dimensions for several different nanoparticle structures resonant at 800 nm would be extremely difficult to perform by hand, and Lumerical FDTD Solutions® software was utilized to enable the process.

Overview of Finite-Difference Time-Domain Method

Lumerical Solutions is, at base, a program that solves Maxwell's equations for a given set of input conditions and structural geometries. It models electromagnetic (EM) interactions in the time domain and uses Fourier analysis to calculate the frequency-dependent response of the geometry. A particular solution region is defined around the given geometry. Within that region, a computational spatial mesh is defined to ensure the greatest accuracy in the regions of greatest interest. This allows the overall simulation area to be divided up into discrete, solvable sections.

The software sets up a system of Maxwell's equations which interweaves the electric and magnetic components and alternates solving each component for each half time-step. In this way, a solution will converge once all sections of the given geometry have continuous solutions that are accurate in both the electric and magnetic components of the field.

Parameters for Resonator Design

When working the nanoscale, every aspect of a device will influence its properties, as shown in the 2014 paper from Stefan Maier's group[12]. This paper discusses the influence on the field enhancement and scattering cross-section of five different factors: the type of metal, the use of an adhesion layer, the substrate, the dimensions and geometry of the antenna, and the use of periodic arrays. Along with these factors, the operational conditions for the device must also be considered before settling on a final design.

For this project, a high-intensity nonlinear laser pulse was used. Therefore, the antenna material needed to have a high thermal tolerance, so that no part of the antenna would be destroyed from the absorbed laser energy. In addition, the substrate needed to be a transparent material, to ensure the only material that would absorb the input light would be the material of which the antennas were composed.

Figure 14 shows the effect that different metals have on the resonant wavelength of a given antenna configuration. The antenna design used for each metal consisted of two disks with a 50 nm diameter and 20 nm thickness separated by a 20 nm gap. For our application, gold was chosen. Even though silver has a slightly larger absorption for this design, gold exhibits less scattering, which means more of the incoming light will be absorbed. (see figure 14 (b)).

Because of the nature of this process established previously in this chapter, a greater absorption will lead to a greater enhancement.
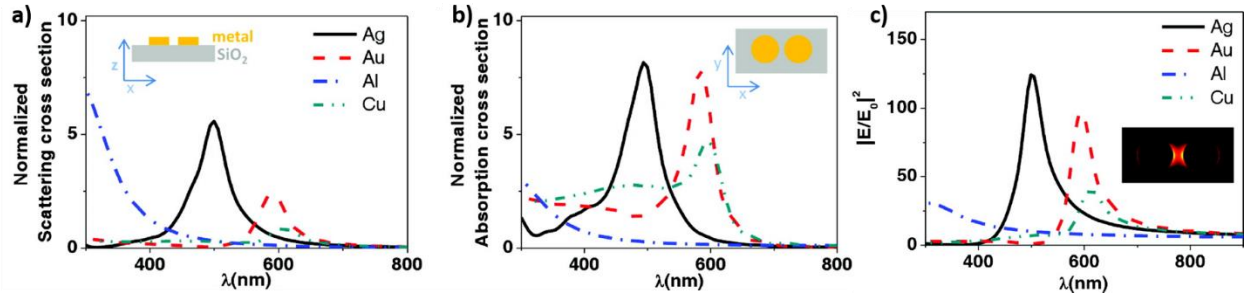
Figure 14: (a) Scattering and (b) absorption cross-sections of dimer antennas made of Ag, Au, Al, and Cu. (c) shows the enhancement generated. All simulations were performed on a semi-infinite silicon dioxide substrate in air[12]. Used with permission.

Figure 15a shows the effect of the substrate on the resonance location. A series of theoretical materials were tested, as well as silicon, gallium arsenide, and germanium. The resonant wavelength of the antenna is gradually shifted to longer wavelengths as the surrounding refractive index increases. Due to the need for a transparent and conductive substrate, glass coated with indium tin oxide (ITO) was chosen as having the refractive index closest to the target resonance wavelength while fitting the other requirements.
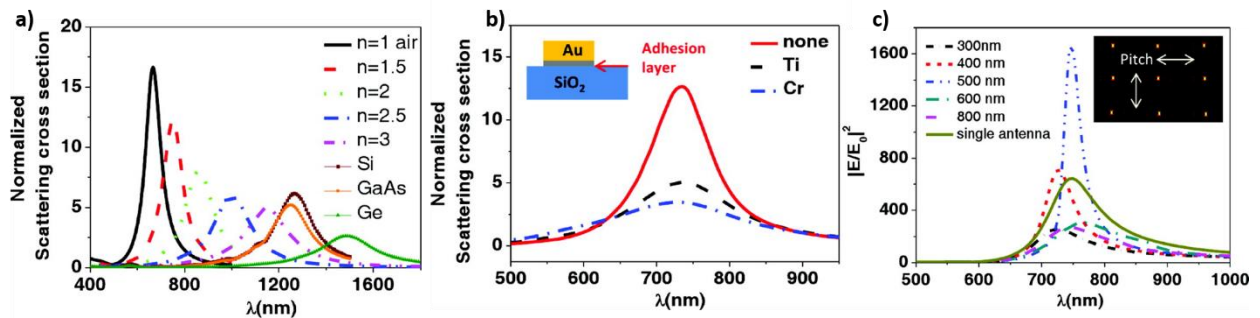
Figure 15: (a) Scattering of plasmonic antenna due to substrate. (b) Scattering of plasmonic antenna due to adhesion layers (c) Scattering of plasmonic antenna due to array size[12]. Used with permission.

Figure 15b shows the effect of adhesion layers. The layer does not cause any significant shift in resonance wavelength, but it does broaden the resonance. Because of this fact, adhesion layers were not used in the simulations or in the fabricated structures. Figure 15c shows the effect of the antennas being organized in an array. Antennas in an array at the proper distance apart (500 nm in this example) will provide an overall enhancement to the resonant intensity. However, the focus of this experiment is on the single antennas, and so while each antenna was simulated as a part of an array, the dimensions between arrays were selected to be large enough that each individual array would not see neighboring arrays.
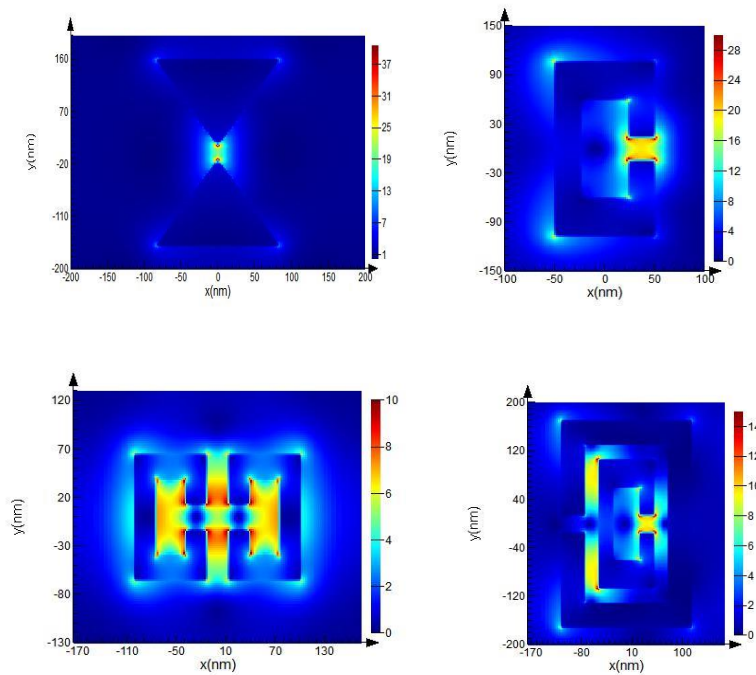
Figure 16: Simulated antenna structures. (a) shows a bow-tie antenna. (b) shows a single split-ring resonator. (c) shows a mirrored split-ring resonator. (d) shows a nested split-ring resonator

With these factors in mind, four different resonators were designed. Two were designed to have relatively simple enhancement patterns (Figure 16, a–b), and the other two were designed to have more complex enhancement patterns (Figure 16, c–d). All structures were simulated with

perfectly matched layers in the *z*-direction, and periodic arrays in the *x*- and *y*-directions. The

simulation region had a mesh accuracy of λ/6, and the fine mesh override had an accuracy of 2

nm. All structures have 40 nm thick gold, and the gold file used was Johnson and Christy[13]. To

reach the final structures, several iterations were run until each structure had a resonance close to

800 nm. The structures shown in Figure 16 are the final antennas designs. All four structures

were fabricated as detailed in Chapter 3.

CHAPTER 3

Methods

In this chapter, we will present a summary of the methodology used to fabricate and analyze the gold nanoantennas studied. The samples are lithographically prepared as described in the "Fabrication" section, then coated with PMMA as described in "Spincoating". The coated nanoparticle arrays are illuminated with a Ti:sapphire laser as described in "Exposure", and prepared for analysis ("Development"). The samples are imaged via scanning electron microscopy ("SEM Imaging"), and analyzed with ImageJ in "Image Processing and Analysis". Finally, the calculations determining the energy applied to the nanoantennas are detailed in "Calculations of Applied Electric Field".

Experimental Methods

Fabrication

We fabricated the nanoparticle arrays at Oak Ridge National Laboratory, using electron-beam lithography. Once the lithography was completed, 40 nm of gold was deposited via resistive (thermal) evaporation. A 1.0 nm/s deposition rate was used for this process. Liftoff was completed using heated PG Remover. The PG remover was heated to 60° C, after which the sample was suspended in the liquid for 20 min. PG remover was then pipetted on the sample to remove large sections of the polymer. The sample was transferred to a beaker of clean PG Remover, also heated, and agitated for 1 minute, then transferred and agitated in beakers of acetone and deionized water. The sample was dried with compressed air to finish the process.

Spincoating

Fabricated arrays were coated with PMMA via spin-coating. Samples were mounted on a plastic disc with an O-ring to provide a vacuum seal and a two-step process was used. The first step spun at 500 RPM for 15 seconds while the polymer was introduced to the substrate, and the second step spun at varying speeds (depending on the desired thickness) for 45 seconds, with rapid acceleration from step one to step two. See Appendix A for table of speed *vs*. thickness.

Exposure

A mode-locked titanium-doped sapphire laser with a wavelength set at 800 nm was used to illuminate the samples. The laser has a repetition rate of 90 MHz and generates 50 fs pulses. Figure 18 shows the schematic for the laser experiment. The generated beam travels through a pair of crossed linear polarizers to provide power control. The pulse then passes through a spatial light modulator. This instrument uses a series of liquid crystals arrays to shape the pulse of the laser according to a designated phase mask. This compresses the pulse to a spectral width of 15 fs. The light is then polarized again and directed through a final lens to focus it onto the arrays with an 8 μm spot size measured by the knife-edge method. A large opaque block is employed to block the laser beam from reaching the sample until it is positioned correctly.

Figure 17: Sample holder for experiment

Coated samples are mounted on a solid metal plate holder (Fig 17) which in turn is mounted on a manually adjustable translation stage. To allow the samples to be positioned spatially, an IR camera is aimed at the sample holder where the beam passes through the sample and a white light source (WLS) is directed onto the sample; this allows the sample to be positioned without damaging the polymer with the laser.
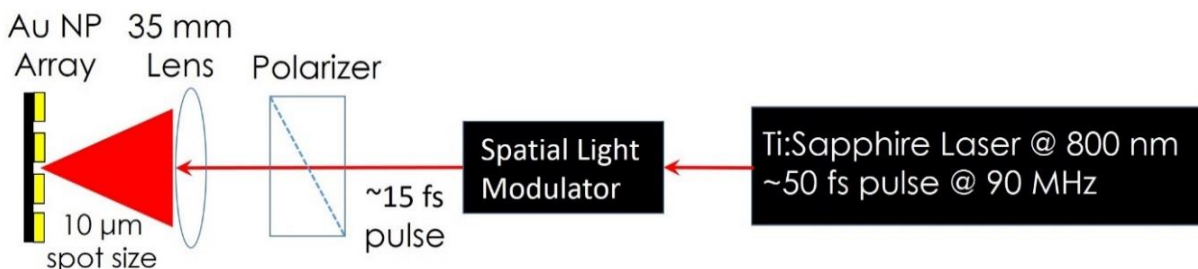
Figure 18: Experimental optical table design. Mode-locked Ti:Sa laser pulse sent through half-wave plate and linear polarizer to provide power control, through Spatial Light Modulator (SLM) to compress pulse to 15 fs, and through final lens to focus pulse onto gold nanoparticle array. An IR camera and a white light source also focused on surface to allow for control over which array was exposed.

Once the sample is positioned, the WLS is turned off and the laser is unblocked for a designated period of time, then re-blocked and the WLS turned back on to allow for repositioning and exposure of the next array.

Development

After exposure, samples were developed to remove the damaged (cross-linked) PMMA using a solution of methyl isobutyl-ketone and isopropyl alcohol in a 3:1 ratio (MIBK:IPA). Samples were held in tweezers and swished through a beaker with 40 mL standard MIBK:IPA solution for 1 minute. They were then thoroughly rinsed with IPA and dried with nitrogen gas.

Analytical Procedures

SEM Imaging

We imaged the developed samples using a Raith Eline scanning electron microscope (SEM). The samples were imaged at 5.00 kV with a working distance of 10 mm. Once images of the damage were captured, the PMMA on the samples was removed via gentle agitation in acetone for 10 minutes and the sample was then dried with nitrogen gas.

Image Processing and Analysis

Collected images were imported into ImageJ, a free image-processing software developed by the National Institute of Health. This software was used to determine all relevant measurements, using the Measure tool. Each measurement is detailed below.

1. Measure of damaged area
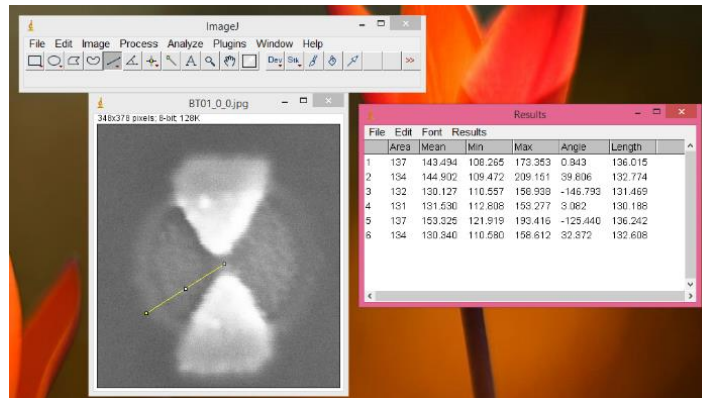
Figure 19: Measurement of damaged area using ImageJ

The radius of the damaged area was measured at six locations around the edge of the circle (see Figure 19). The start point was on the edge of the circle, and the end point was taken to be the mid-point of the gap. The six measurements were then averaged to get the final radius, which was used to calculate the damaged area.

2. Measure of gap size
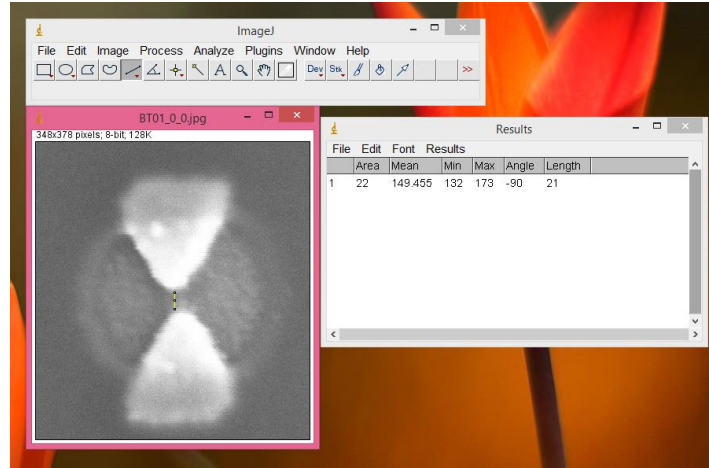
Figure 20: Measurement of gap size

The gap between the antennas was traced out from the tip of the bottom antenna to the bottom of the top antenna, with care being taken to keep the measurement perpendicular between the start and end point. When the two tips were not collinear, the gap was taken to be the vertical distance between the two tips.

3. Measure of triangle area
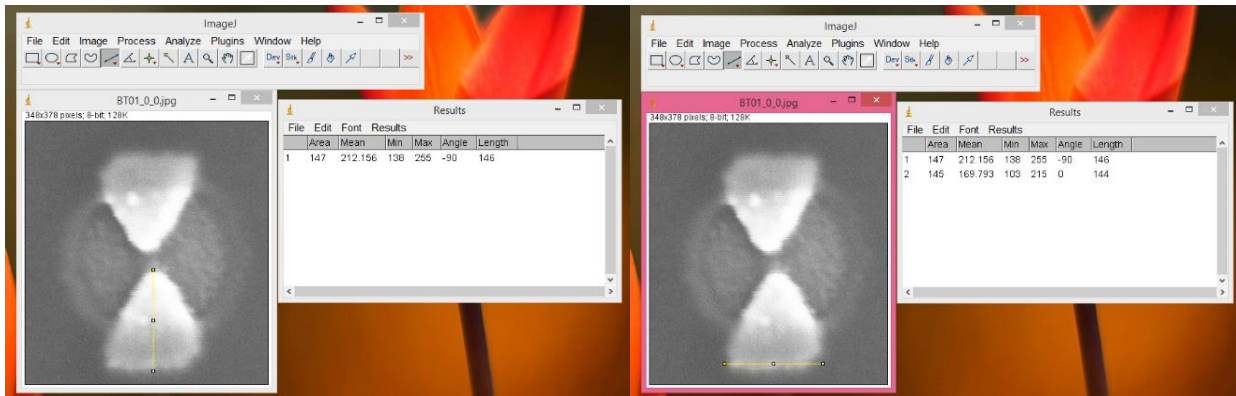
Figure 21: Measurement of triangle base and height dimensions

The triangle areas were calculated by measuring the base and the height of each triangle. The height was measured from the tip of the triangle straight down to the base, and the base was determined by measuring at the widest point of the triangle.

Calculate Applied Electric Field

To calculate the electric field generated by each laser pulse, it was necessary to calculate the peak power applied by the laser multiplied by the pulse duration. This value is used to determine the electric field generated by a laser pulse. The laser power was measured with a power meter near the focal point of the laser. This was then converted to the electric field. First, the average power measured was converted to the peak power using Eqn 8:

$$P_{peak} = \frac{P_{avg} \cdot \tau}{T} \qquad\qquad \text{Eqn 8}$$

Where τ = the pulse duration and T= the period of the laser. From that value, equation 9 was used to calculate the electric field:

$$|E| = \sqrt{\frac{2 \cdot P_{peak}}{A \cdot c \cdot \varepsilon_0 n}} \qquad\qquad \text{Eqn 9}$$

Where A= area of the laser spot, c= vacuum speed of light, and n= refractive index of the medium. The typical peak power applied was 30 mW, and the typical peak intensity was 60 GW/cm^2.

CHAPTER 4

Results and Discussion

The first goal of these experiments was to replicate Quidant's results with nanorods to ensure that the experimental setup was correctly designed. Figure 22 shows several of the SEM images of nanorods collected. Column a shows the original SEM images, column b shows the images with the damaged region highlighted, to make it easier to discern, and column c shows the specific parameters for each individual nanorod.

Each nanorod in this experiment was designed to be 50 nm wide with varying lengths. The antennas were exposed to three different intensities for the same length of time. Figure 22 shows all three intensities and five different nanorod lengths.

a.   **b.**

140 nm, 10 mW, 30 s
Peak intensity = 20 GW/cm²

140 nm, 40 mW, 30 s
Peak intensity = 81 GW/cm²

150 nm, 30 mW, 30 s
Peak intensity = 61 GW/cm²

160 nm, 30 mW, 30 s
Peak intensity = 61 GW/cm²

180 nm, 30 mW, 30 s
Peak intensity = 61 GW/cm²

190 nm, 10 mW, 30 s
Peak intensity = 20 GW/cm²

Figure 22: Damaged nanorods. (a) shows the nanorods as imaged in the electron microscope. (b) shows the nanorods with the damaged areas highlighted

Due to the inherent challenges of nanoscale fabrication, no pattern can be reproduced perfectly; each nanoscale feature will have some variance. This is illustrated neatly with the top

two nanorods in Figure 22. Both are designed to have precisely the same dimensions, yet they appear quite different due to minor, unavoidable variations in the fabrication process. However, when studying resonant structures, this becomes an advantage. Distin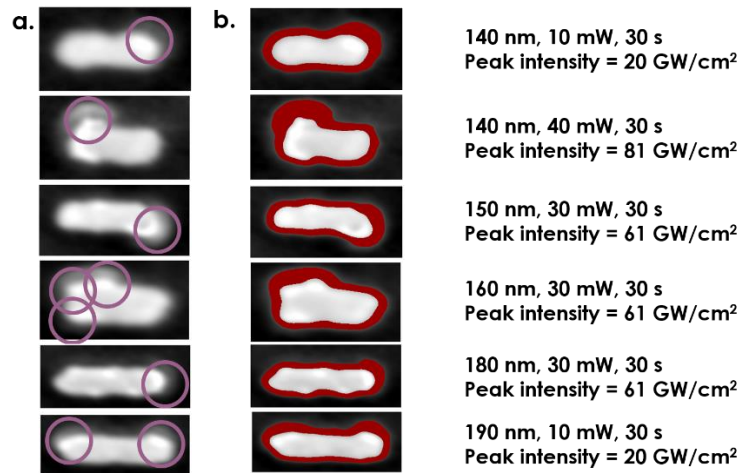ct features such as sharp corners can concentrate electric fields, and the stronger the electric field the stronger the stronger the effect on the PMMA. In the case of this experiment, a stronger effect means a larger amount of damaged area. The six nanorods in Figure 22 all have these distinct features, which have led to a discernable section of damage associated with them. The first nanorod is slightly larger on the right-hand side, and this is reflected in the increased damage seen surrounding that side. The second nanorod likewise has one major feature, but on the top left side of the particle. This region of damage is much easier to see for two reasons. First, the location of the feature causes the damage to be made outside of the natural resonance pattern for the antenna and second, the nanorod was exposed with a much higher light intensity of light. The third and fifth antennas are similar to the first antenna; there is a single feature close to the end of the nanorod which enlarged the usual damaged region. The fourth antenna has three features all at one end of the nanorod, and this caused an extended region of damage to form. The last antenna has two features, one at each end, and has regions of greater damage to correspond with them.

The first results proved the experiment done by Quidant et al. was repeatable, but it was difficult to move beyond qualitative analysis of the results. The features created by variations in fabrication provide interesting regions to observe but are irregular enough to make it challenging to determine any kind of relationship between antenna and damaged region. A further experiment was designed to determine the quantitative nature of this method. Bowties were selected for two reasons: to further demonstrate the applicability of the technique to a wide range of structures, and to increase the ease of relating the input intensity to the output enhanced field.

The bowtie structure, as previously discussed, has a very simple enhancement pattern, which

makes measurement of the damaged area much more straightforward.
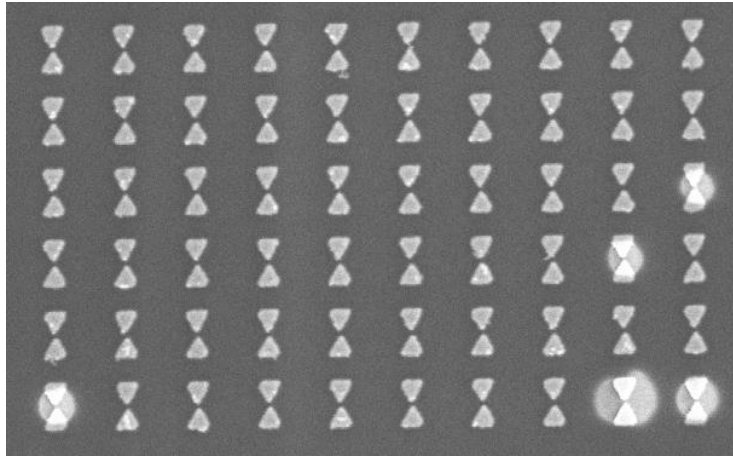
Figure 23: Array of bowtie antennas. Five antennas in this array responded to the input light.

Figure 23 shows an array of bowtie antennas. This array was illuminated with a Gaussian

beam of light at 800 nm and 30 mW intensity for 30 seconds. The laser spot size was 10 μm, so

the 4μm by 6μm array fit entirely inside the focal spot and every antenna was irradiated with the

same intensity within a factor two. However, only five of the sixty antennas in this array reacted

to the application of light. This reinforces the idea that the effect relies on a resonance and

depends on a specific geometry for the antennas. Therefore, we began our analysis by examining

the geometry of the five antennas that reacted and eight representative antennas that did not.
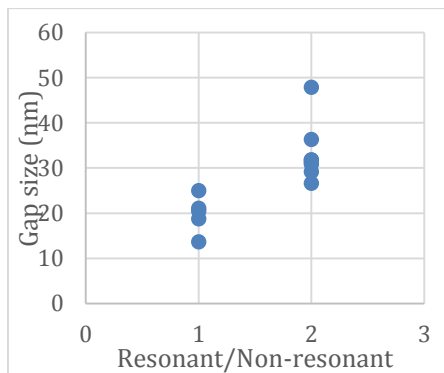
Figure 24: Gap between two antennas, sorted between resonant (1) and non-resonant (2)

As stated previously, the precise geometry of an optical device can have a strong impact on its functionality. For a bowtie antenna, the most critical parameter is the distance between the two triangles (referred to as the gap size hereafter). Figure 24 shows the various measured gap sizes for the antennas under study, sorted to show if they were resonant or non-resonant without reference to strength of resonance. It is readily apparent that the distance between the two triangles has a strong impact on whether or not the antenna reacted to the input light. The reason for this is simple: if the two triangles are too far apart, they will not "see" one another, and the resonance will be unable to form.
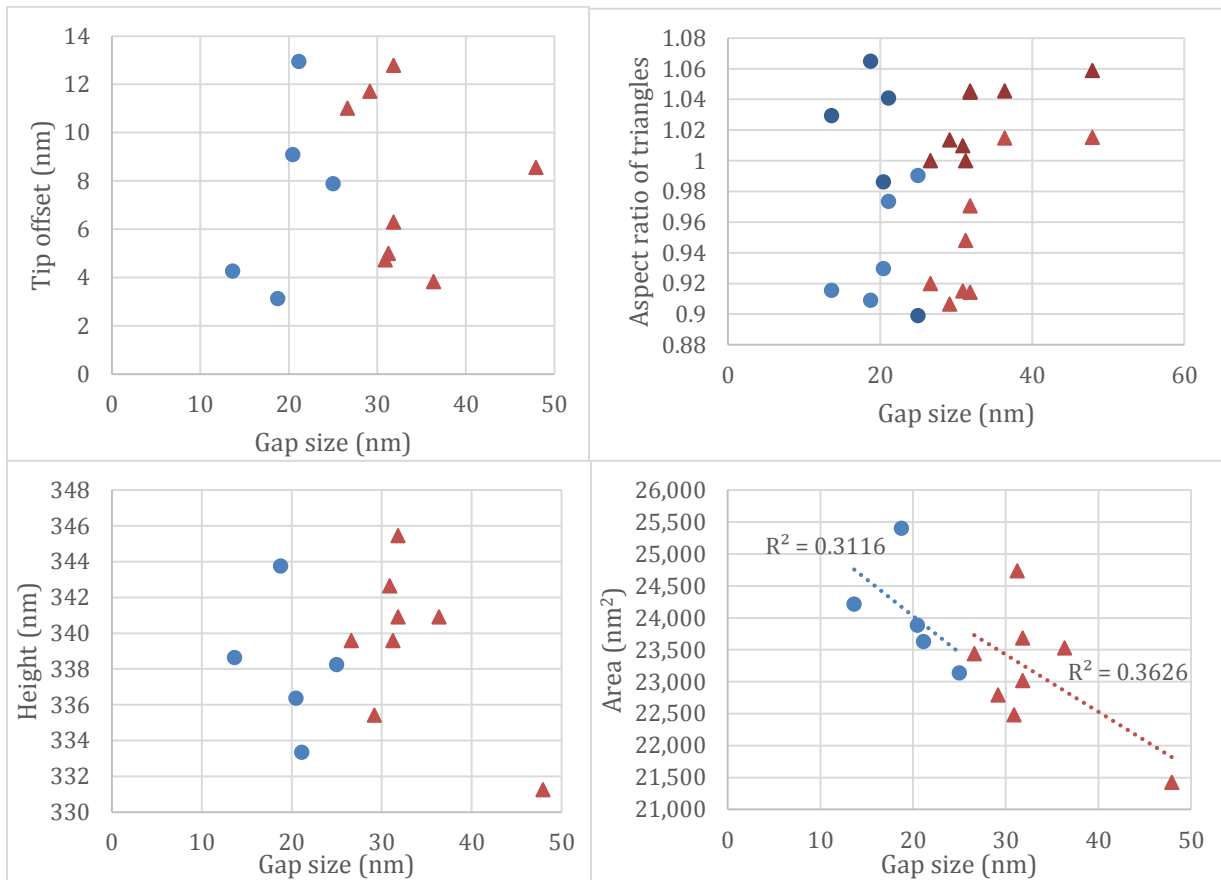
Figure 25: (a) shows the size of the offset between the two triangles of the bowtie antenna, sorted between resonant antennas and non-resonant antennas. (b) shows the aspect ratio for the individual triangles of the antennas, (c) shows the total heights of the antenna, and (d) shows the total area of the antenna. The blue circles represent the antennas which were resonant. The red triangles represent the antennas which were non-resonant.

While the gap distance is the most critical parameter for a two-particle antenna, a selection of parameters for the bowtie antennas was examined to see which might also have an impact on the resonance. To determine if the secondary parameters were also correlated to resonance, they were plotted against the gap size. Fig 25a) shows the offset of the tips of the two triangles in the antenna, 25b) shows the aspect ratio for the component triangles, 25c) shows the total heights of the metal in the antenna, and 25d) shows the total area of the antenna. Looking at the displayed trends, a few things can be observed. The R^2 that fits the gap vs the total area is around 0.3 for both the resonant and the non-resonant antennas. This means that the ratio of the area to the gap size is also roughly correlated to the occurrence of resonance vs. non-resonance. Likewise, the aspect ratio might be correlated to resonance. The other two parameters do not appear to have predictive potential.

With a basic understanding of which parameters cause the antennas to be resonant, the next step is attempting to replicate this in simulations. In building these simulations, it was discovered that the metal antennas did not remain unchanged through the time period of the experiment. The measured gap size increased by around 15 nm. This was likely caused either by repeated polymer deposition and removal or by laser ablation at the edges of the gap due to high laser intensity. The solution agitation to remove the polymer can cause small particles of metal to be flaked off along with the polymer, and this can gradually decrease the size of the nanoparticle. Enough repeated deposition and removal cycles can lead to a noticeable change in the overall dimensions of the nanoparticle.
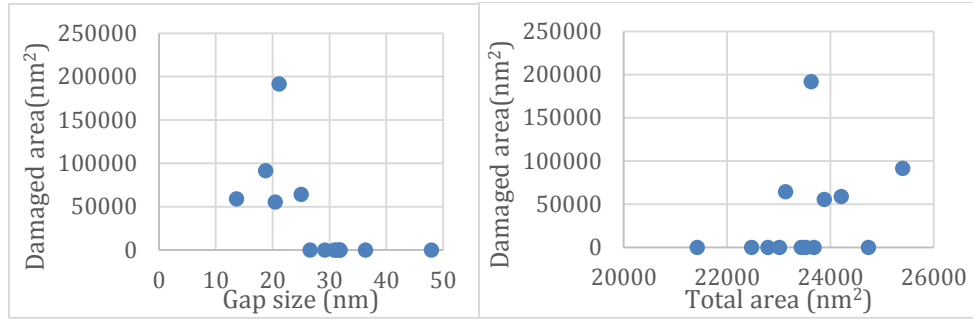
Figure 26: (a) gap size vs. damaged area. (b) total area vs. damaged area

Figure 26 shows the two parameters of interest plotted against the experimental damage area. Once again, gap size shows the possibility of a trend. This sets up our expectations for the simulation results: the antennas which generated a damage circle will have a greater electric field strength than the antennas which did not. As well, the antennas with a smaller gap size and with a larger total area will have a greater electric field strength.
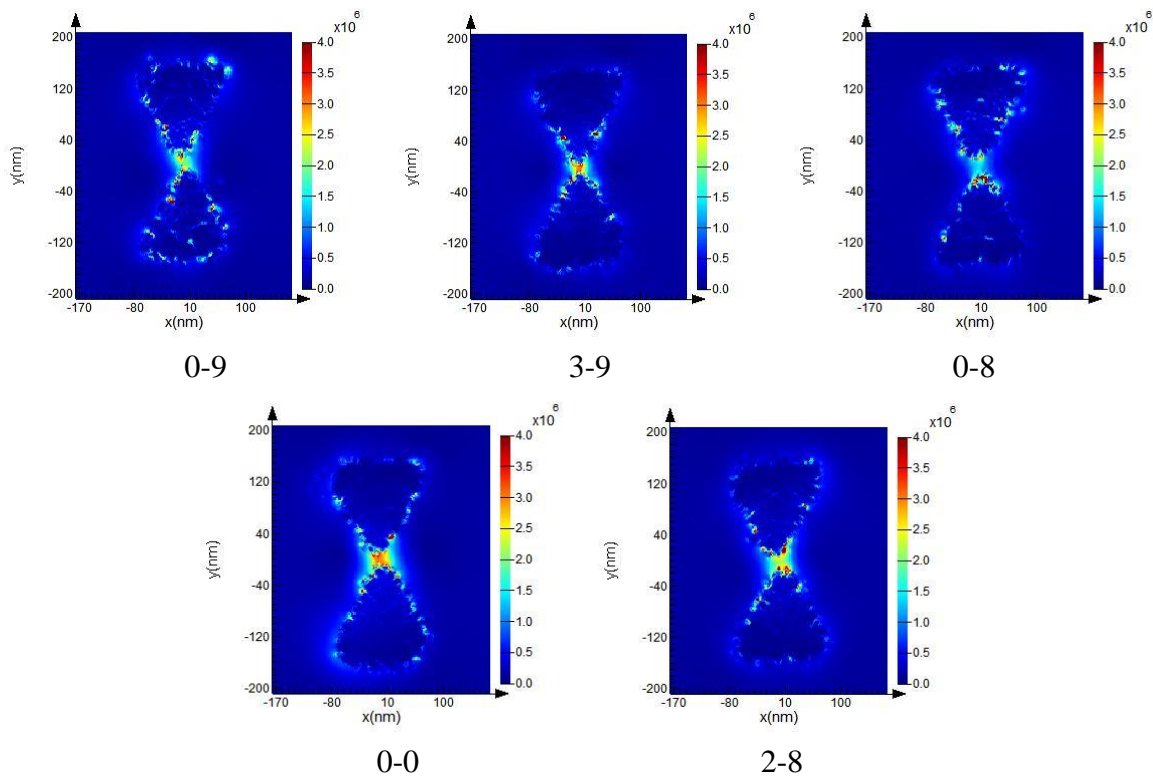
Figure 27: Simulated bowtie antennas. These five are the antennas that generated damaged areas.

33

Figure 27 shows the electric field maps for the five bowtie antennas which resonated in the experiment, while Figure 28 shows the electric field maps for eight non-resonant bowtie antennas. All of the scales for the plots have been set to a maximum electric field at 4.0×10^6 V/m. This allows for a more straightforward comparison between the various antennas. It also allows us to disregard the hotspots formed due to the structure import processes that are not really present.

0-1   2-9   3-7

2-7   1-8   1-7

0-7   1-9
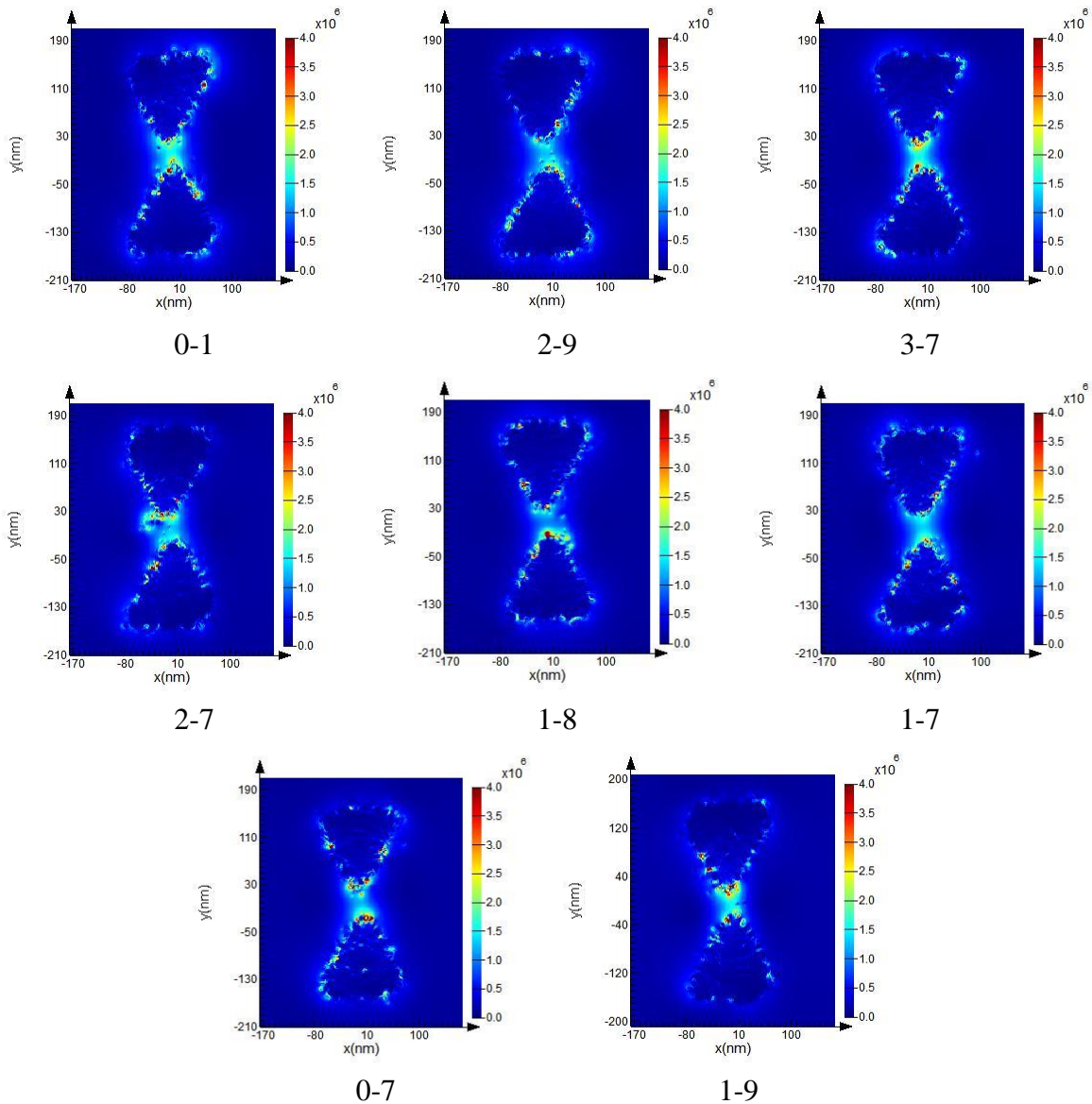
Figure 28: Simulated bowtie antennas, non-resonant

Immediately it can be seen that *in general*, the first expectation is met: the antennas which were resonant do generate a greater electric field than the antennas that were not. However, this is also not uniformly true. The calculated electric field across the gap for antenna BT-08 is weaker than many of the fields in the non-resonant antennas.

Figure 29 quantifies the differences in electric field strength by giving the enhancement factor of the antennas. Four of the resonant antennas have an enhancement factor greater than 12. The non-resonant antennas all have an enhancement factor between 6 and 9. Once again, in general terms this makes sense: polymers have a breakdown strength that must be exceeded for any visible damage to be observed. The simulation data support our theory that gap size affects electric-field strength, and that a threshold electric field enhancement must be reached before damage can be seen.

The general expectation breaks down most notably on one antenna: BT-08. This antenna not only resonated in the experimental results, it was the antenna with the largest generated damaged area. However, in the simulations, it only generated an enhancement factor of 8.39, a number solidly in the middle of the non-resonant enhancements. The enhancement factors for the other antennas likewise do not align with the observed damaged areas. BT-39 has the greatest enhancement factor of the simulated antennas, but has the second smallest measured damage, indicating a much smaller enhancement factor experimentally.
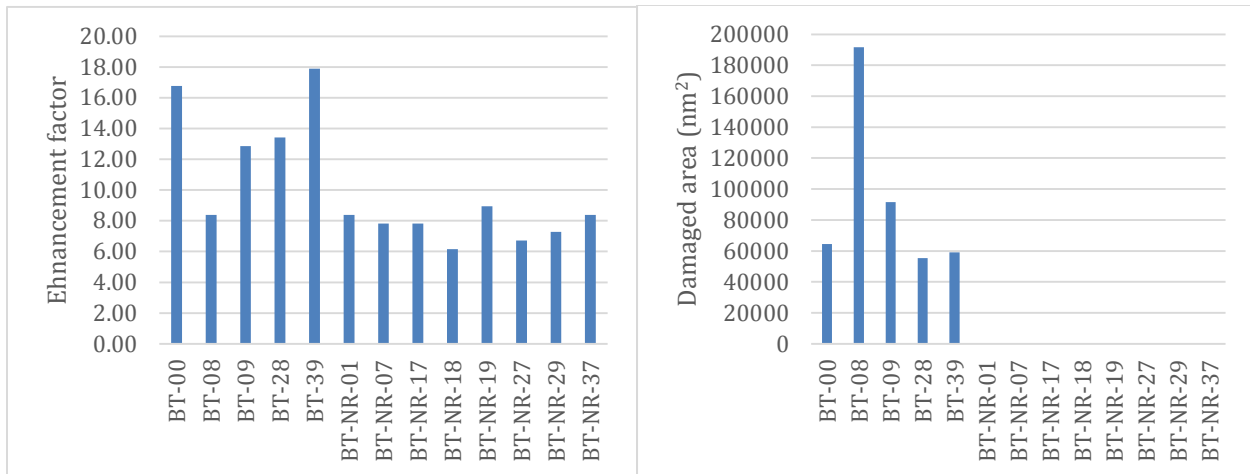
Figure 29: (a) Calculated enhancement factor for each simulated antenna at 800 nm. (b) Damaged area generated by each experimental antenna

It is unclear why this is occurring, but there are several possibilities. Resonant antennas have a wavelength band over which they will generate the largest response. As described previously, PMMA is damaged in this wavelength region through nonlinear means, namely through absorption by the gold nanoparticles and generation of the fourth harmonic. Because of this, the transmission curve for the antenna can tell us in which wavelength ranges we can expect to see the greatest generated electric field.
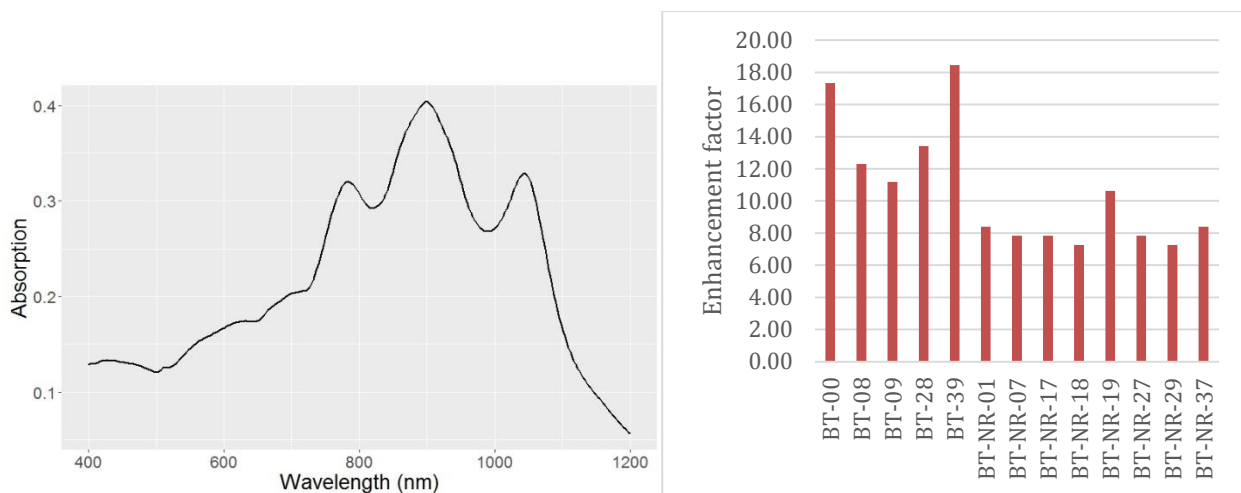
Figure 30: (a) Absorption curve for antenna BT-08. (b) Calculated enhancement factors for each simulated antenna at 825 nm

36

Figure 30 a) shows the absorption spectrum for antenna BT-08. We see that the greatest absorption, and therefore the greatest expected enhancement, comes at a longer wavelength than the simulations were run. However, this does not play out consistently across the remaining antennas. The expected enhancement factors at 825 nm also do not replicate the experimental results well, as seen in Fig 30 b). Antenna BT-08 is no longer one of the lowest-enhanced resonators, but neither is it the largest. The other antennas also do not have a good match for the observed enhancement. While we have clearly showed that there is a threshold for polymer damage, we have not been able to identify the precise relationship between gap size, antenna shape, and generated electric field intensity.

CHAPTER 5

Conclusions

In replicating the work from the ICFO, we were able to show that near-field mapping is a viable technique to analyze a variety of optical resonators. We then moved on to use the technique in an exploratory examination of plasmonic bowtie antennas. From this we were able to learn that the most critical parameters in predicting if a bowtie antenna will be resonant appear to be the distance between the two antennas (the gap size) and the ratio of total surface area of metal included in the resonator to the gap size. These two conclusions are logical due to the method by which this process works: the metal nanoparticle absorbs the incoming photons and re-emits the fourth harmonic of that wavelength, which damages the surrounding polymer by a dielectric breakdown mechanism. More metal in the nanoparticles means more incoming light will be absorbed and a greater response will be observed. As well, when the two triangles of the bowtie antenna are closer together, they will interact more and the field generated by each nanoparticle will be greater. Several other parameters were examined that do not appear to have an effect on whether or not the antennas were resonant: the total height of the antenna, the offset of the tips of the two triangles, and the aspect ratio of the component triangles. The aspect ratio might have an impact on the existence of a resonance, but we cannot determine that with the antennas fabricated for this experiment.

Future Work

Our experiments have led us to draw some preliminary conclusions, but it is clear that this complex system is not yet fully understood. The simulations performed did not exactly replicate our experimental results, indicating that there is some additional mechanism occurring within the system that was not included in the setup for the simulation. It is possible that one of the parameters examined and thought to not have significance will prove to have a greater impact than believed. The place to start, therefore, is in exactly replicating the bowtie experiments. A greater amount of data will greatly assist in creating an exact model of a single resonant bow-tie antenna. It will allow us to determine with greater certainty that the size of the gap between the two triangles, the area of the triangles themselves, and the shape of the triangles are factors that contribute to the antenna being resonant or not resonant.

For the experiments described here, the Ti:sapphire oscillator was in a standard oscillator mode. This laser also has a cavity-dumping option where it produces femtosecond pulses in the 20-25 nJ range at a pulse repetition frequency (prf) of 200 kHz. This contrasts with the oscillator pulses at 96 MHz prf which have only 3-5 nJ energy per pulse. This opens up an additional avenue of experimentation by permitting a significant variation in local intensity. We believe that providing a greater energy per pulse at a lower pulse repetition frequency will lead to being more able to consistently excite the resonance in the antennas.

Another needed task for taking this project forward is making precise measurements of the light reflected off of the array and the light transmitted through the array, so the exact amount of light being absorbed by the antennas can be calculated. Due to the nature of the array, this measurement is not trivial. It will be important to know the energy being imparted to the antenna so the simulations generated will be accurate.

Once an exact simulation model for the bow-tie antenna has been made and the ideal conditions for generating the most consistent excitations have been determined, we can move on to determining the precise link between the energy absorbed and therefore emitted from the bow-tie and the area that the emitted energy damages. This link is of upmost importance for this technique to gain widespread use as an analytical tool. It would allow for experimenters to measure the electric field strength generated by a device as it is being constructed, rather than having to wait for all steps of fabrication to be completed to make measurements of how a device functions. Because the damage occurs only in the polymer, a device can be tested without ruining it, so that if it turns out to be good, fabrication can be completed with no loss. To accomplish this, one set of antennas should be excited at a variety of intensities. Each intensity would generate a different amount of damaged polymer, from which an equation could be determined relating the strength of the electric field generated by the antenna to the amount of damaged polymer it creates. Once the link between electric field and damaged polymer is established, it could be tested on more complex resonant systems to verify if it is robust. With this relationship determined, this technique could provide a quantitative measure of the strength of the electric field generated by a plasmonic structure rather than just a qualitative picture.

Two final related directions of potential future work can be noted, with each using this technique in a quite different manner. One of the current challenges of nanoscale engineering is how to make small features accurately, rapidly, and precisely located. Near-field mapping could be used to solve several of those problems at once.

The first use of this technique is quite straightforward. When the laser damages the polymer and that damaged polymer is removed chemically, it leaves a hole in the polymer, exactly as would happen when preparing a sample after performing lithography. The hole in the

polymer could then be filled by any standard deposition method. This would allow for the formation of composite nanoparticle systems, such as the structure needed for a perfect absorber[14]. By tuning the original nanoparticle antenna design and the power applied, a range of inner nanoparticle sizes could be formed. There are several challenges that would need to be solved with this direction. The most critical is the chance that the depth of the void created might not reach all the way to the substrate. This is not a problem for the imaging use of this technique, but would cause the deposition to fail. The other notable challenge would be to determine the correct laser intensity to apply to generate the proper size of interior nanoparticle. This would be much easier with the equation relating applied field to generated damage size.

The other direction from this research has a much broader set of potential applications. While in this document we have simplified our analysis and treated the electric fields generated by plasmonic antennas as two dimensional, the emitted field exists in the z-direction as well. Taking this into account would allow us to leverage the technique to create small periodic arrays of nanoparticles. An array of metallic bowtie nanoparticles could be fabricated on a transparent substrate and mounted on a fixed arm. The target substrate would have a given thickness of polymer deposited on it and mounted on a movable arm. This arm would then be brought into near contact with the fixed arm holding the existing nanoparticle array. The bowtie antenna array would be then be excited, and the generated fields would damage the polymer on the moveable arm. This arm would then be pulled back, the substrate removed and developed, and the process continued as in any traditional lithography process.

Some of the same challenges that apply to the previous direction also apply here. The precise laser intensity to be applied would have to be carefully calibrated to ensure the desired size of nanoparticle could be obtained. Because the field is emitted in a spherical pattern, the

distance between the fixed target plate and the movable patterned plate would have to be taken into account when determining the power needed. Since the substrate to be patterned is not the same as the one with the existing nanoparticles, there is less of a restriction on the depth of polymer that the emitted field must penetrate. This means that underdevelopment is less of a concern for this direction than in the previous direction.

The main additional challenges for this technique exist with the fixed target plate. As we have seen already, it is extremely challenging to make consistently sized objects when fabricating devices at the nanoscale. However, once made, the plate should be good for extended use as there would be no need to continually spin and remove polymer from it. This should greatly extend the life of the antenna array as a template. The substrate for the fixed plate provides the other challenge. As the technique stands, the light to excite the plasmonic resonance will need to travel through the substrate onto the particles. Great care will be required when selecting the material for the substrate to ensure that the light does not interact with the substrate when passing through it.

PMMA mapping has many different potential applications. The primary application is as an analytical technique for determining the location of electromagnetic near fields on a device. It allows for the fields to be observed visually on a device without causing any damage to the device itself, and for fabrication or use of the device to continue after analysis is complete. It also has potential for use as a fabrication technique. Further work is highly recommended to pursue this technique.

REFERENCES

1. in *The Economist* (http://www.economist.com/news/business/21648683-microchip-pioneers-prediction-has-bit-more-life-left-it-ever-more-moore, 2015).

2. A. M. Fox, *Optical Properties of Solids*, 2nd ed. (Oxford University Press, United States, 2010).

3. D. R. Smith, W. J. Padilla, D. C. Vier, S. C. Nemat-Nasser and S. Schultz, Physical Review Letters **84** (18), 4184-4187 (2000).

4. D. W. Pohl, W. Denk and M. Lanz, Appl. Phys. Lett. **44** (7), 651-653 (1984).

5. F. C. de Lange, Alessandra; Huijbens, Richard; de Bakker, Barbel; Rensen, Wouter; Garcia-Parajo, Maria; van Hulst, Niek; Figdor, Carl G, J Cell Sci **114** (2001).

6. M. Bosman, V. J. Keast, M. Watanabe, A. I. Maaroof and M. B. Cortie, Nanotechnology **18** (16) (2007).

7. J. Nelayah, M. Kociak, O. Stephan, F. J. Garcia de Abajo, M. Tence, L. Henrard, D. Taverna, I. Pastoriza-Santos, L. M. Liz-Marzan and C. Colliex, Nature Physics **3** (5), 348-353 (2007).

8. E. J. R. Vesseur, R. de Waele, M. Kuttge and A. Polman, Nano Lett. **7** (9), 2843-2846 (2007).

9. P. Leiderer, C. Bartels, J. Konig-Birk, M. Mosbacher and J. Boneberg, Appl. Phys. Lett. **85** (22), 5370-5372 (2004).

10. G. Volpe, M. Noack, S. S. Acimovic, C. Reinhardt and R. Quidant, Nano Lett. **12** (9), 4864-4868 (2012).

11. H. Jiang and R. Gordon, Plasmonics **8** (4), 1655-1665 (2013).

12. R. Fernandez-Garcia, Y. Sonnefraud, A. I. Fernandez-Dominguez, V. Giannini and S. A. Maier, Contemporary Physics **55** (1), 1-11 (2014).

13. P. B. Johnson and R. W. Christy, Physical Review B **6** (12), 4370-4379 (1972).

14. W. Li and J. Valentine, Nano Lett. **14** (6), 3510-3514 (2014).